HHS Public Access

Author manuscript

Neuron. Author manuscript; available in PMC 2022 May 09.

Published in final edited form as:

Neuron. 2021 August 18; 109(16): 2545–2555.e7. doi:10.1016/j.neuron.2021.06.010.

Dual metabotropic glutamate receptor signaling enables coordination of astrocyte and neuron activity in developing sensory domains

Vered Kellner[1], **Calvin J. Kersbergen**[1], **Sally Li**[1], **Travis A. Babola**[1], **Gesine Saher**[2], **Dwight E. Bergles**[1,3,4,*]

[1]The Solomon H. Snyder Department of Neuroscience, Johns Hopkins University, Baltimore, MD, 21205, USA

[2]Department of Neurogenetics, Max Planck Institute of Experimental Medicine, Göttingen, 37075, Germany

[3]Department of Otolaryngology Head and Neck Surgery, Johns Hopkins University, Baltimore, MD, 21205, USA

[4]Kavli Neuroscience Discovery Institute, Johns Hopkins University, Baltimore, MD, 21205, USA

Summary

Astrocytes play an essential role in the development of neural circuits by positioning transporters and receptors near synapses and by secreting factors that promote synaptic maturation. However, the mechanisms that coordinate astrocyte and neural maturation remain poorly understood. Using *in vivo* imaging in unanesthetized neonatal mice we show that bursts of neuronal activity passing through nascent sound processing networks reliably induce calcium transients in astrocytes. Astrocyte transients were dependent on intense neuronal activity and constrained to regions near active synapses, ensuring close spatial and temporal coordination of neuron and astrocyte activity. Astrocyte responses were restricted to the pre-hearing period and induced by synergistic activation of two metabotropic glutamate receptors, mGluR5 and mGluR3, which promoted IP3R2-dependent calcium release from intracellular stores. The widespread expression of these receptors by astrocytes during development and the prominence of neuronal burst firing in emerging neural networks may help coordinate the maturation of excitatory synapses.

Keywords

Auditory system; astrocyte; spontaneous activity; mGluR; brain development

[*]Corresponding author and lead contact: Dwight E. Bergles, PhD, The Solomon H. Snyder Department of Neuroscience Johns Hopkins University School of Medicine 725 N. Wolfe Street, Baltimore, MD 21205, USA, P:410-955-6939, dbergles@jhmi.edu.

Author contributions

Conceptualization, V.K. and D.E.B; Methodology, V.K., C.J.K., S.L., T.A.B.; Investigation, V.K., C.J.K., S.L., T.A.B.; Providing reagents, G.S.; Formal Analysis, V.K., C.J.K., S.L., T.A.B.; Writing – Original Draft, V.K. and D.E.B.; Writing – Review & Editing, V.K., C.J.K., S.L., T.A.B. and D.E.B.; Funding Acquisition, V.K., T.A.B., C.J.K., and D.E.B.

Declaration of interests

D.E.B. is a member of the scientific advisory board of Decibel Therapeutics.

Introduction

Prior to the onset of sensory experience, correlated groups of neurons in peripheral sensory organs, assigned to discrete sensory domains, fire periodic bursts of action potentials that propagate through sensory processing centers in the CNS (Blankenship and Feller, 2010). Spontaneous correlated firing among neurons mapped to similar sensory space provides a means to induce refinement of synapses through Hebbian mechanisms. This intrinsically generated activity is conserved among species, extremely resilient to perturbations and required for precise maturation and refinement of neuronal circuitry (Clause et al., 2014; Xu et al., 2011). However, the mechanisms by which this early patterned activity initiates these diverse cellular and synaptic changes remain poorly understood.

Although neurons have been the primary focus of studies of developmental activity (McLaughlin et al., 2003; Tritsch et al., 2010), astrocytes are also critical elements of excitatory synapses. Immature astrocytes appear within the parenchyma shortly after neurons (Bayer and Altman, 1991) and extend thin lamellar sheets from their highly ramified processes (Bushong et al., 2004; Freeman, 2010) that place glutamate transporters near sites of release and provide a barrier to diffusion, limiting synaptic crosstalk (Bergles and Jahr, 1997). The elaboration of astrocyte processes is initiated at a time when nascent synapses are established and refined (Ullian, 2001), suggesting that their development is closely coordinated, ensuring the specificity of information transfer and preventing runaway excitation. Astrocytes have also been shown to secrete factors that promote the formation, maturation and refinement of excitatory synapses (Clarke and Barres, 2013), but little is known about the activity patterns of astrocytes in the developing CNS *in vivo* or the temporal and spatial relationship between neuronal and astrocyte activity during this critical phase of synaptic refinement.

Neurons in the developing auditory system exhibit high frequency bursts of action potentials prior to the onset of hearing (Lippe, 1994; Tritsch et al., 2007), ensuring robust postsynaptic activation to allow signal propagation from the cochlea to the auditory cortex. Burst firing is ideally suited to produce large glutamate transients that promote engagement of receptors outside the synaptic cleft (Scanziani et al., 1997), a phenomenon that is likely to be enhanced in the developing CNS due to the limited ramification of astrocyte processes (Bushong et al., 2004) and lower expression of glutamate transporters (Sutherland et al., 1996). During this early developmental phase, astrocytes express metabotropic glutamate receptors (Sun et al., 2013) that are optimized for detecting focal glutamate transients, but the context in which these receptors are engaged in developing circuits are unknown.

Here, we examined astrocyte activity patterns in nascent circuits within the mouse auditory system prior to the onset of hearing. We found that groups of neighboring astrocytes within future isofrequency zones in the developing inferior colliculus (IC) exhibited periodic, highly correlated calcium transients that were aligned both temporally and spatially with bands of neuronal activity. Astrocyte calcium increases were induced by coincident activation of metabotropic glutamate receptors mGluR5 and mGluR3 following neuronal burst firing, and exhibited a higher threshold, narrower spatial extent and more prolonged timecourse than neuronal events. This coordinated activation of neurons and astrocytes

in future isofrequency zones disappeared after hearing onset. These results indicate that intrinsically generated neuronal burst firing during development activates astrocytes within discrete sensory domains, providing a means to coordinate the spatial and temporal maturation of neurons and astrocytes at excitatory synapses.

Results

Correlated neuronal and astrocyte activity in the developing CNS

To define astrocyte activity patterns in the developing CNS, we performed time lapse fluorescence imaging in mice that expressed the genetically encoded calcium indicator GCaMP3 under control of the promoter/enhancer for GLAST (*GLAST-CreER;ROSA26-lsl-GCaMP3*; hereafter termed *GLAST;GC3* mice) (Figures S1A and S1B). Cranial windows were implanted over the midbrain of young postnatal mice (P7–11) to visualize the superior and inferior colliculi (SC, IC), where neurons exhibit prominent burst firing at this age (Ackman et al., 2012; Babola et al., 2018; Tritsch et al., 2010) due to spontaneous activity generated in the retina and cochlea, respectively. Imaging was performed using a widefield fluorescence microscope in awake (unanesthetized) pups, enabling macroscopic patterns of activity to be monitored simultaneously across brain hemispheres (Figure 1A). Time lapse imaging revealed that groups of astrocytes in these regions exhibited transient, spatially restricted increases in intracellular calcium that were distinct between auditory (IC) and visual (SC) regions (Figure 1B); astrocyte activity in SC propagated as broad continuous waves, whereas activity in IC was organized into discrete bands (Movie S1). Here, we focused primarily on the IC to expand our knowledge of cellular activity patterns in the auditory pathway prior to hearing onset.

In comparison to the spontaneous bursts of neuronal activity in P7 *Snap25-T2A-GCaMP6s* mice (Babola et al., 2018), astrocyte calcium transients were smaller, less frequent and longer in duration (Figures 1C and 1D); however, like neuronal activity, astrocyte responses in IC were often mirrored across the brain, with discrete events occurring simultaneously in both left and right IC. Comparable activity patterns were observed when astrocytes expressed GCaMP6s (*Aldh1l1-CreER;R26-lsl-GCaMP6s*) (Figures 1C and S1C–G), indicating that these distinct features of astrocyte activity were not due to expression of different calcium indicators. Similarly to neurons (Babola et al., 2018), astrocyte calcium transients were dependent on cochlear input, as ablation of the left cochlea completely abolished spontaneous astrocyte events in the right IC, visible in both the map of summed activity, the loss of dominant events and the dramatic decrease in frequency of events in the right IC (Figures S2A and S2B). Astrocyte activity bands were sometimes restricted to the central region (Figure 1E, *Event 1*) and at other times formed doublets at the margins (Figure 1E, *Event 2*), but were consistently aligned perpendicular to the tonotopic axis, oriented diagonally when viewed from the dorsal surface (see Figure 1B). In *Snap25-T2A-GCaMP6s* mice just after hearing onset (P14–16), exposure to low (3 kHz) and higher (15 kHz) frequency tones elicited similar bands of activity in IC neurons (Figure 1E) (Babola et al., 2018), indicating that astrocytes within this developing auditory center exhibit periodic, highly correlated activity aligned to future isofrequency domains.

To visualize astrocyte and neuron activity patterns at high resolution simultaneously, we performed two photon imaging in mice that expressed GCaMP3 in astrocytes and jRGECO1a, a red-shifted calcium indicator, in neurons (*GLAST;GC3;Thy1-jRGECO1a* mice). Using a custom grid-based analysis that automatically detects active regions (see Methods) (Movie S2), spontaneous activity was assessed in continuous five-minute segments from P7–8 mice. This analysis revealed that astrocyte events were spatially and temporally correlated with neuronal events in the same region (Figure 1F and 1G), with 91 ± 3% of active astrocyte grids overlapping with active neuronal grids (n = 80 events, 5 mice, $p < 0.01$ versus random overlap); however, the peak of astrocyte calcium transients was delayed 1.7 ± 0.3 s (Figure 1H), spatially restricted (Figure 1I *Left*), and longer in duration than neuronal events (Figure 1I *Right*). Although astrocyte events invariably followed bands of neuronal activity in the same area, most neuronal events (92%) were not associated with detectable increases in astrocyte calcium. Neuronal events that preceded astrocyte events were larger in area, longer in duration and had higher amplitudes than neuronal events not associated with astrocyte activity (Figure 1J; N(+A) compared to N), suggesting that astrocytes have a higher threshold for activation. Together, these results indicate that large amplitude spontaneous neuronal events are spatially and temporally correlated with astrocyte activity in this central auditory center prior to hearing onset.

Astrocyte calcium activity in the auditory cortex

Spontaneous bursts of neuronal activity that originate in the developing cochlea prior to hearing onset propagate through nascent auditory pathways to reach auditory cortex (AC) (Babola et al., 2018). To determine if neuronal burst firing is also capable of inducing astrocyte activity in isofrequency domains of the AC at this age, we used macroscopic widefield imaging in P6–8 *GLAST;GC3* mice to simultaneously monitor astrocyte calcium levels in IC and AC (see Methods) (Figure 2A); AC was identified by local vascular morphology and subsequent correlation of activity patterns between IC and AC (Figure 2A). Time lapse imaging revealed that astrocytes in AC also exhibited periodic increases in calcium. These events were slightly smaller in amplitude than responses in IC (Figure 2B and 2C), and while the events in IC and AC were highly correlated (Pearson's $\rho = 0.81 \pm 0.02$, n = 8 mice), the temporal delay between events in IC and AC was less apparent compared to neuronal events (Babola et al., 2018), presumably because of the slower rise time and prolonged duration of astrocyte calcium increases. Using the tonotopic organization of IC as a guide, individual IC events were used as a seed to map corresponding active areas in AC (Figure 2D). Astrocytes within AC also exhibited spatially restricted activation that segregated according to the known tonotopic organization (Figures 2D and 2E). These results indicate that astrocytes in developing auditory midbrain and cortex exhibit periodic correlated activity within isofrequency lamina in concert with bursts of neuronal activity.

Astrocyte coordinated events diminish after hearing onset

Spontaneous neuronal burst firing first emerges in the auditory system during the late prenatal period, increases in frequency during the first two postnatal weeks, and then ceases just after hearing onset (Babola et al., 2021; Tritsch et al., 2010). To determine the developmental profile of astrocyte coordinated calcium activity, we used widefield imaging

of the AC in P4, P7, P11 and P14–15 *GLAST;GC3* mice. Astrocyte activity closely followed developmental changes in neuronal burst firing; very few calcium events were detected at P4, at P7 and P11 astrocyte calcium events were robust, and these events declined again just after hearing onset (P14–15) (Figure 2F). To explore the link between neuronal and astrocyte activity in hearing mice, we monitored sound-evoked calcium responses in the AC of dual indicator mice (*Aldh1l1;GC6s; Thy1-jRGECO1a*) (Figure 2G). Although neurons in these mice responded robustly to a range of frequencies and sound pressure levels in a characteristic tonotopic pattern (Figure 2G, *left panel* and 2H), astrocytes in AC did not respond to even loud tonal stimuli (100dB SPL) (Figure 2G, *middle panel* and 2H), although they exhibited broad activation when the animals moved (Figure 2G, *right panel*). These findings are consistent with the observation that astrocytes in the adult visual cortex (V1) do not exhibit calcium increases in response to visual input, but are activated in response to norepinephrine release during heightened states of arousal (Paukert et al., 2014). Thus, large scale coordinated activity in neurons and astrocytes is restricted to a narrow developmental time period prior to the onset of sensory experience.

Astrocyte calcium events are mediated by mGluR5

Astrocytes in the developing cortex express mGluR5 metabotropic glutamate receptors, Group I G_q-coupled receptors that generate IP3 and release calcium from internal stores (Sun et al., 2013; Zhang et al., 2014). To determine if astrocyte calcium transients in the IC were dependent on IP3R2, we imaged *GLAST;GC3;IP3R2*$^{-/-}$ mice, which have been shown to exhibit profoundly reduced neurotransmitter evoked calcium transients in astrocytes (Petravicz et al., 2008). Correlated astrocyte calcium transients were completely absent in these mice (Figure S3), indicating that global astrocyte activity at this age depends on metabotropic receptor induced release of calcium from intracellular stores. To determine if astrocytes in the developing IC also express mGluR5 receptors, we performed time lapse confocal imaging in acute slices of midbrain from P7-P9 *GLAST;GC3* mice and applied. In the presence of antagonists to block action potential firing (see Methods), the Group I mGluR agonist DHPG (10μM) reliably elicited a rise in calcium within IC astrocytes (Figures S4A and S4B) that was abolished by the mGluR5 antagonist MPEP (10μM; Figure S4C). To determine if correlated astrocyte events *in vivo* require activation of mGluR5 receptors, we performed widefield imaging of astrocytes in the IC before and after intraperitoneal injection of MPEP (10mg/kg). MPEP administration blocked tonotopically organized astrocyte calcium signals in the IC almost immediately, while injection of vehicle alone did not alter astrocyte activity (Figures 3A and 3B; Movie S3). In contrast, MPEP had no significant effect on either the frequency (Figure 3C and 3D) or amplitude of neuronal events in *Snap25-GC6s* mice (amplitude difference, %ΔF/F: vehicle, 0.22 ± 0.3; p=0.47; MPEP, 0.4 ± 0.2; p=0.42, Paired t-test, n = 4 and 5 mice, vehicle and MPEP, respectively), suggesting that the decrease in astrocyte activity was not due to suppression of neuronal burst firing. To address the specific role of astrocyte mGluR5 receptors, we generated an astrocyte specific knockout of mGluR5 by crossing *mGluR5*$^{fl/fl}$ mice (Xu et al., 2009) to *Aldh1l1-CreER;GC3* mice (mGluR5 cKO) and inducing recombination by injecting 4-hydroxytamoxifen at P1–2 (see Methods). Astrocytes in acute IC slices from mGluR5 cKO mice no longer responded to DHPG with a calcium rise, although norepinephrine (10μM) still elicited a robust increase in calcium (Figures S4D and S4E), indicating

that calcium release mechanisms remained intact. Widefield imaging in P7 mGluR5 cKO mice pups revealed that spontaneous astrocyte calcium transients in IC were abolished in these mice, indicating that astrocyte mGluR5 receptors are necessary to induce these coordinated, spatially-restricted events (Figures 3E and 3F). Thus, neuronal burst firing in the developing auditory pathway engages mGluR5 receptors in nearby astrocytes, eliciting correlated calcium transients within specific isofrequency lamina.

Astrocyte calcium events also require mGluR3 receptors

Astrocytes in the developing brain also express mGluR3 (Sun et al., 2013; Zhang et al., 2014)., a G_i-coupled Group II mGluR previously linked to calcium rises in astrocytes (Moldrich et al., 2002; Winder and Conn, 1993), suggesting that it could also be activated through neuronal burst firing. In acute IC slices from P7–11 *GLAST;GC3* and *Aldh1l1;GC6s* mice, the Group II agonist LY354740 (1μM; in TTX, 1μM) elicited a comparable rise in calcium in astrocytes in the central nucleus and external cortex of the IC, (number of responsive grids: p=0.65; the integral of response: p=0.86, Student's t-test, n = 4 slices/area, 4 mice) (Figures S4F) that was inhibited by the mGluR2/3 antagonist LY341495 (100μM), although these responses were more variable than DHPG in the proportion of astrocytes responding (Figure S4G). To determine the contribution of mGluR3 to coordinated activation of astrocytes *in vivo*, we imaged P7–10 *GLAST;GC3* pups before and 30 minutes after systemic administration of LY341495 (3mg/kg). Similar to the effect of mGluR5 inhibition, LY341495 abolished astrocytic calcium events in the IC (Figures 4A and 4B; Movie S4), suggesting that mGluR3 activation is also required to generate astrocyte calcium transients. Although modulation of neuronal mGluR2/3 receptors could contribute to this effect (Petralia et al., 1996), mGluR2/3 antagonism is expected to enhance, rather than suppress glutamate release (Mateo and Porter, 2007; Xi et al., 2002). *In vivo* macroscopic imaging in *Snap25-GC6s* mice revealed that LY341495 unexpectedly decreased the amplitude of neuronal responses in IC by 16 ± 0.8 % (n = 7 mice; $p < 0.001$), but had no effect on event frequency (p = 0.9) (Figure 4C and 4D). To study the role of astrocytic mGluR3 without possible complications of manipulating neuronal receptors, we generated *Aldh1l1-CreER;mGluR3$^{fl/fl}$;GC6s* (mGluR3 cKO) mice to selectively remove mGluR3 from astrocytes. Widefield imaging in awake P7–9 mGluR3 cKO mice revealed that both the amplitude and frequency of spontaneous astrocyte calcium transients were reduced relative to controls (Figures 4E–H; 48.5 ± 3 % decrease in frequency; $p < 0.05$; 21 ± 6% decrease in amplitude; $p < 0.05$; n = 7 mice). The residual activity was not dependent on mGluR3, as systemic administration of LY341495 did not further reduce event frequency (Figure 4H Left, compare to Figure 4B) or amplitude (Paired t-test; p = 0.3, n = 4 mice), but was dependent on mGluR5 (Figure 4H Right). Together, these results indicate that synergistic activation of two distinct metabotropic glutamate receptors, mGluR5 and mGluR3, contribute to calcium rises within astrocytes in response to neuronal burst firing in the auditory system prior to hearing onset.

Discussion

Synergistic activation of metabotropic glutamate receptors in astrocytes

mGluRs were first shown to induce intracellular calcium changes in astrocytes in dissociated cultures from the developing brain (Cornell-Bell et al., 1990; Nedergaard, 1994; Porter and McCarthy, 1995), extending initial reports that astrocytes express glutamate gated ion channels (Barres et al., 1990) and providing key evidence that glial cells could be directly influenced by neurotransmitters. Nevertheless, although long suspected to be a primary means of neuron-astrocyte communication in brain circuits, *in vivo* evidence of physiological activation of mGluRs in astrocytes has remained elusive. In the adult CNS, astrocytes in the cerebral cortex exhibit global increases in cytosolic calcium when norepinephrine is released during periods of heightened arousal (Ding et al., 2013; Paukert et al., 2014), as well as spontaneous, microdomain calcium transients within their processes (Grosche et al., 1999; Srinivasan et al., 2015) that arise, in part, from mitochondrial calcium release (Agarwal et al., 2017). Subsequent studies revealed that mGluR5, the primary Gq-coupled mGluR responsible for glutamate induced calcium transients in astrocytes (Cai et al., 2000; Wang et al., 2006), is downregulated by these cells with increasing postnatal age (Cai et al., 2000; Sun et al., 2013), providing an explanation for the inability to observe astrocyte calcium changes in response to local synaptic activity in the adult mouse CNS. Our studies reveal that astrocytes in the developing midbrain and cortex express functional mGluR5 receptors that enable detection of spontaneous bursts of neuronal activity that course through emerging sensory pathways.

Although mGluR5 has been a primary focus of glutamate-induced calcium signaling in astrocytes, mGluR3 is also expressed by these cells from early development into adulthood (Sun et al., 2013). This Group II mGluR is linked to G_i-mediated inhibition of adenylate cyclase and reductions in cAMP in most cells (Tanabe et al., 1993); however, traditionally G_i coupled receptors, including mGluR3 and heterologous inhibitory DREADD receptors, also induce calcium increases in astrocytes by promoting release from intracellular stores (Durkee et al., 2019; Winder and Conn, 1993). Nevertheless, physiological activation of mGluR3 in astrocytes has not been established *in vivo*. We find that conditional deletion of mGluR3 from astrocytes and *in vivo* pharmacological inhibition of mGluR3 reduced neuron-induced calcium transients in astrocytes in the developing brain, indicating that concurrent activation of mGluR3 and mGluR5 predominates in astrocytes at this age. These receptors act synergistically, as suppression of mGluR5 signaling alone abolished neuron-induced calcium increases in astrocytes, consistent with recent studies showing that mGluR3 potentiates mGluR5-induced calcium transients in developing pyramidal neurons and enhances polyphosphoinositide (PI) hydrolysis by mGluR5 in cortical slices from early postnatal mice (Di Menna et al., 2018). Interactions between these two receptors may occur early in the signal transduction pathway, through G_q activation of phospholipase C by $\beta\gamma$ subunits liberated from mGluR3 (Wang et al., 1999). The persistent expression of mGluR3 into maturity by astrocytes raises the possibility that it may continue to act in a synergistic role with other G_q-coupled receptors to enhance normally subthreshold responses. In primary visual cortex of adult mice, light-induced activation of neurons only reliably triggers local astrocyte activity during periods of heightened arousal, when

norepinephrine is released (Paukert et al., 2014; Slezak et al., 2019). Synergistic interactions between mGluR3 and G_q-coupled alpha adrenergic receptors similar to that described here could enhance mGluR3 signaling in mature astrocytes to enable detection of local circuit activity.

Possible consequences of astrocyte calcium signaling in the developing brain

Astrocytes undergo a dramatic morphological transformation in the postnatal mouse brain (Bushong et al., 2004), a process facilitated by neuroligin-neurexin signaling with neurons (Stogsdill et al., 2017), in which they elaborate fine processes that place transporters and ion channels near sites of release for efficient neurotransmitter and potassium clearance, and enable neuromodulation through release of gliotransmitters (Araque *et al.*, 2014). Studies of developing astrocytes *in vitro* indicate that focal glutamate application can induce filopodial outgrowth from astrocyte processes (Cornell-Bell et al., 1990; Lavialle et al., 2011) and VGluT1-KO mice exhibit reduced astrocyte morphological complexity *in vivo* (Morel et al., 2014), raising the possibility that mGluRs link intracellular calcium changes to morphogenesis and stabilization of tri-synaptic structures. Astrocytes have also been shown to secrete factors that promote the development (e.g. Thrombospondins; Christopherson et al., 2005; Eroglu et al., 2009), maturation (e.g. Glipicans and Chordin-like 1; Allen et al., 2012; Blanco-Suarez et al., 2018) and refinement of synapses (MertK, Megf10; Chung et al., 2013). Although elevation of intracellular calcium can induce changes in gene expression (Ghosh and Greenberg, 1995), cell dynamics (Zheng and Poo, 2007) and secretion (Araque et al., 2000; Katz and Miledi, 1967) in a variety of cells, and has been linked to a decrease in GABA transporter expression in striatal astrocytes (Yu et al., 2018), the downstream consequences of these periodic calcium transients remain to be defined.

Astrocytes co-cultured with neurons increase their expression of GLT-1 (EAAT2), a glutamate transporter responsible for the majority of glutamate uptake in the adult CNS (Swanson et al., 1997), in an mGluR5-dependent manner (Yang et al., 2009) and conditional knockout of mGluR5 from astrocytes reduced ensheathment of excitatory synapses and GLT-1 expression (Morel et al., 2014), pointing to an important role for developmental mGluR5 signaling in promoting the structural and functional maturation of astrocytes. The activity patterns described here may help coordinate neuronal and astrocyte maturation within discrete, functionally important networks dedicated to processing information from similar aspects of sensory space. The high threshold for astrocyte activation, in which only a subset of the largest neuronal burst events trigger calcium rises in astrocytes, may limit spurious activation of highly amplifying metabotropic receptors, and increase the probability of interactions through engagement of multicellular astrocyte and neuronal networks. Although these studies were focused on the auditory system, burst firing is a characteristic feature of diverse neural networks during development (Kirkby et al., 2013). Our observation of coordinated activation of astrocytes in the superior colliculus, mirroring the pattern of neuronal activity induced by retinal waves (Ackman et al., 2012), suggests that coincident astrocyte-neuron activity may have a conserved role during early development of the CNS.

STAR METHODS

Resource availability

Lead contact for reagent and resource sharing—Requests for sharing resources and reagents should be directed to the Lead Contact, Dwight Bergles (dbergles@jhmi.edu).

Materials availability—This study did not generate new unique reagents.

Data and code availability—All imaging data reported in this paper will be shared by the lead contact upon request. All original code has been deposited on github (https://github.com/Bergles-lab/Kellner-et-al.--2021-source-code) and is publicly available as of the date of publication. Any additional information required to reanalyze the data reported in this paper is available from the lead contact upon request.

Experimental model and subject details—Male and female mouse pups between the ages of P4 to P11 were used in experiments prior to hearing onset and P14–15 after hearing onset. Gender was a random variable. Mice were maintained on a mixed background to improve litter survival and to mitigate potential effects of C57BL/6 mutations involved in hearing. Since we used an inducible Cre-loxP system for all experiments involving astrocytes, experimental mice were injected with tamoxifen (see Tamoxifen injections section below). Mice were housed on a 12-hour light/dark cycle and were provided food ad libitum. All experiments and procedures were approved by the Johns Hopkins Institutional Care and Use Committee.

Transgenic Animal Models—Generation and genotyping of the following mouse lines: *GLAST-CreER* (Wang et al., 2012), *Aldh1l1-CreER* (Winchenbach et al., 2016), *ROSA26-lsl-GCaMP3* (Paukert et al., 2014), *ROSA26-lsl-GCaMP6s* (Kim et al., 2016), *Snap25-T2A-GCaMP6s* (Madisen et al., 2015), *Thy1-jRGECO1a-WPRE* (GP8.62; Dana et al., 2016), $IP3R2^{-/-}$ (Li et al., 2005), and $mGluR5^{fl/fl}$ mice (Xu et al., 2009) have been previously described. $Grm3^{tm1a(KOMP)Wtsi}$ mice were acquired from KOMP and crossed to *ROSA26-FLPe* mice to generate $Grm3^{fl/fl}$ mice. *ROSA26-lsl-GCaMP6s* in which the neo cassette was removed using *ROSA26-FLPe* mice were also utilized.

Method Details

Tamoxifen Injections: The tamoxifen solution for injections (1 mg/mL) was freshly prepared by sonicating tamoxifen (T5648, Sigma-Aldrich) in sunflower seed oil (S5007, Sigma-Aldrich) at room temperature for 20–30 min (with intermittent 20 s vortexing every 10 min). This solution was stored at 4°C for 5–7 days away from light. In *Aldh1l1-CreER;ROSA26-lsl-GCaMP6s*, $Aldh1l1\text{-}CreER;mGluR5^{fl/fl}$ and $Aldh1l1\text{-}CreER;mGluR3^{fl/fl}$ mice and their controls, (Z)-4-Hydroxytamoxifen (4-OHT; H7904; Sigma-Aldrich) was used. To prepare 4-OHT, powder was dissolved in 100% EtOH to achieve a final concentration of 20 mg/ml. Stock aliquots containing 50 µl were made and stored at −80° until needed. When needed, 250 µl of sunflower seed oil was added to the aliquot, and sonicated for 20–30 min (with intermittent 20 s vortexing every 10 min). The solution was then spun using a speed vacuum to ensure evaporation of the EtOH and used

within 24hrs. Mice were injected intraperitoneally (i.p.) with 50 μl of tamoxifen (50 ng per animal) or 4-OHT (200 μg per animal) between P1-P3 (unless otherwise mentioned in the text), once a day for two consecutive days, with each injection a minimum of 20 hrs apart.

Installation of cranial windows: The surgery was described previously in Babola et al., 2018. Briefly, animals were anesthetized with isoflurane (3–4% for induction, until mice were unresponsive to toe-pinch and 1–2% during the procedure). Following a local injection of lidocaine, a midline incision was made and the scalp was removed. A head bar was secured to the head using super glue (Krazy Glue). Connective tissue and muscles were either cut or pushed away above the interparietal bone. HEPES-buffered artificial cerebrospinal fluid (HEPES-aCSF) was applied to the exposed bone and replenished throughout the surgery. The interparietal bone was removed to expose the midbrain. The dura mater was removed, exposing the colliculi and extensive vasculature. A 5mm coverslip (CS-5R; Warner Instruments) was placed over the craniotomy, the surrounding bone was dried and super glue sealed the coverslip to the skull. Post-surgery, 0.9% NaCl solution was injected subcutaneously and lidocaine was injected to the back of the neck. The isoflurane was discontinued and the pups were placed under a warming lamp, for a minimum of 1 hour prior to imaging. After imaging was completed, all animals were euthanized and in some cases the brain was harvested.

For simultaneous imaging of inferior colliculus (IC) and auditory cortex (AC), in addition to the above procedure for IC, a cranial window over AC (~3.5 mm lateral to lambda) was made, starting from the lateral suture and moving medially (~3 to 4 mm diameter). The dura was carefully removed before a 4mm glass coverslip (CS-4R; Warner Instruments) was glued over the window. Auditory cortex windows in P14-P15 mice were installed using a microblade and microscissors to remove musculature and a ~3 mm circular region of skull overlying the right auditory cortex. Following skull removal, the dura was carefully removed using microscissors and exposed brain was continuously immersed in HEPES-aCSF. A 5 mm coverslip (CS-5R; Warner Instruments) was attached using super glue, and animals were allowed to recover a minimum of 2 hours prior to imaging.

Cochlear ablation: Prior to cranial window installation, a postauricular incision was made and the cervical musculature retracted to expose the auditory bulla. The bone enclosing the auditory bulla was removed and the middle ear exposed. Using fine forceps, middle ear mesenchyme was removed to expose the cochlear wall. Using a small-diameter aspirator, the bony cochlear wall was perforated and the cochlea removed. The open cavity was packed with Gelfoam to prevent bleeding, the overlying muscles moved back into place, and the incision sealed with Vetbond. Animals were imaged within 3 hours after the procedure. After imaging, a cochlear dissection was performed to ensure complete ablation. Animals with incomplete ablations or mice in which there was no calcium activity in the contralateral IC or in the SC (superior colliculus) were not used for analysis.

***In vivo* calcium imaging:** After recovering from anesthesia for 1–3 hours, pups were mounted onto a metal bar to ensure head-fixation. They were maintained at 37°C by using a heating pad during the imaging (TC-1000; CWE). The pups were mostly calm during imaging sessions but occasional movements occurred. These movements were detected

and removed during image processing (see below). After hearing onset (~P12), awake animals were imaged while head-fixed but on a freely-rotating tennis ball to simulate natural movement.

Widefield epifluorescence imaging was performed using a Hamamatsu ORCA-Flash4.0 LT digital CMOS camera coupled to a Zeiss Axio Zoom V16 stereo zoom microscope. For midbrain imaging, a 4×4mm field of view was illuminated continuously with a metal halide lamp (Zeiss Illuminator HXP 200C) and visualized through a 1X PlanNeoFluar Z 1.0x objective at 17x zoom. When simultaneously imaging the cortex and the midbrain, a 6×6mm field of view was obtained using a 11x zoom. Image resolution was 512×512 pixels (16-bit pixel depth) after 2×2 binning to increase sensitivity. Imaging sessions consisted of uninterrupted acquisition over 10 minutes with an acquisition frame rate of 10 Hz, unless otherwise noted.

For dual-color two-photon imaging of neurons and astrocytes with single-cell resolution, a two-photon microscope (Zeiss LSM 710) was used. Two photon excitation was achieved using a Ti:sapphire laser (Chameleon Ultra II; Coherent) tuned to 1000 nm. A 425×425 μm or 607×607 μm field of view was visualized using a 20x Zeiss 1.0 NA objective. Images were collected at a resolution of 512×512 pixels (8-bit pixel depth) at 2 Hz using a galvo-galvo scanner.

Sound stimuli: Acoustic stimuli were presented using a free-field speaker (MF1; Tucker Davis Technologies) placed 10 cm from the left ear within a custom sound attenuation chamber with external noise attenuation of 40 dB (Babola et al., 2018). Stimuli consisted of 4 repetitions of cosine-gated sinusoidal amplitude modulated pure tones (1 s, 10 Hz modulation) from 3 to 48 kHz in ¼ octave intervals played in a random order at 5 s intervals. Tones were generated within the RPvdsEx software (Tucker Davis Technologies), triggered using the microscope's frame out signal, and delivered through the RZ6 Audio Processor (Tucker-Davis Technologies). Calibration of the free-field speaker was performed using a calibrated microphone (7017; ACO Pacific, Inc.) and preamplifier (4016; ACO Pacific, Inc.) in BioSigRZ software (Tucker-Davis Technologies). Given the relatively flat intensity profile of the speaker (peak amplitude 105 dB SPL ± 5 dB for a 2.0 V stimulus at tested frequencies from 3 – 50 kHz), stimulus levels were not corrected across presented frequencies. Stimuli for displayed images and analysis were presented with zero attenuation (105 ± 5 dB SPL) because of high auditory thresholds around ear canal opening.

Drug delivery: For *in vivo* drug delivery, the animals were imaged as described above and then injected intraperitonially with either MPEP (10 mg/kg; Tocris; dissolved in ddH2O), an mGluR5 antagonist, LY341495 (3 mg/kg; Tocris; dissolved in 1.2eq NaOH and diluted in 0.9% NaCl), an mGluR2/3 antagonist, or vehicle (ddH2O or 0.9% NaCl). The animals were imaged immediately after injection (in the case of MPEP and ddH2O) or within 30–60 min after injection (in the case of LY341495 and 0.9% NaCl).

Image processing: Widefield videos were visually inspected for clarity of the window and for superior colliculus (SC) activity. If the window was obstructed by blood or there was no SC activity, the movie would not be processed further. In some cases, either

the right or left IC was clear and the movie was processed only for that side. Animals that had undergone cochlear ablation and KO animals often did not have SC activity but were still used for data analysis. Widefield raw images were imported into MATLAB (MATHWORKS) and corrected for photobleaching by subtracting a fitted exponent from the signal. Images were cropped to include only the inferior colliculus (IC) and a square area in the middle of the IC was used to detect auto fluorescent signals. Movement was detected using efficient subpixel image registration (Guizar-Sicairos et al., 2008) and the signal was zeroed during the detected movement events (after filtration, see below). Image intensities were normalized as $\Delta F/F_o$ values, where $\Delta F = F - F_o$ and F_o was defined as the median over all frames. Ovoid regions of interest (ROIs) encompassing the entire left and right inferior colliculi were drawn (see Figure 1B). The size of the ROIs was mostly constant across animals but ROI locations were manually chosen due to variations in the imaging field. The calcium trace was then smoothed and filtered by regressing the baseline over multiple shifted windows using a spline approximation (‘msbackadj’ function in MATLAB, window and step size - 5 frames). Peaks in the signals were detected in MATLAB using the built-in peak detection function (‘findpeaks’) using a fixed value threshold criterion (1% $\Delta F/F_o$). This method detected the most prominent peaks in both astrocytes and neurons. Peaks were then visually inspected to ensure that they were spatially restricted to the tonotopic organization of the IC and not due to movement. Movement related peaks were manually removed. For presentation of movies, the bleach corrected images were run through an algorithm for structured low-rank matrix factorization (Haeffele et al., 2014). The components were visually inspected and those that showed mainly vascularization were removed. The movies were also pseudo-colored in Fiji (Schindelin et al., 2012). No analysis was performed on these movies, they were for display purposes only.

For two-photon imaging of astrocyte and neurons simultaneously, images were imported into Fiji for presentation. The red and green channels were split and were used for further processing in MATLAB. For presentation purposes, each movie was filtered using a Gaussian blur method (radius = 0.5–1). Brightness and contrast were also adjusted as needed. For analysis in MATLAB, the raw signal was used. Grid ROIs were defined as 25×25 pixels over the entire image, resulting in 400 ROIs for each movie. The calcium trace for each ROI was filtered by regressing the baseline over multiple shifted windows using a spline approximation (‘msbackadj’ function in MATLAB, window and step size - 45 frames). To define responsive grid ROIs, peaks in the signal were detected using the built-in ‘findpeaks’ function in MATLAB. The threshold was defined as the median + MAD (median absolute deviation) of each ROI’s signal for neurons and as the median + 3xMAD (median absolute deviation) for astrocytes. These thresholds were manually defined and corroborated for each animal. Events were defined when a peak was detected in at least 10 grids. The events were then visually inspected and manually determined based on the best fit of the grids to the movie. The overlap between astrocyte and neuronal events was determined by having the user draw a polygon around the events and measuring how many astrocyte grids were overlaid compared to all astrocyte grids for that event. The active neuronal grids were then randomly shuffled (using ‘randblock’; 200 times and the overlap was tested for each repetition. Significance was determined by counting the number of times the shuffled data was larger than the measured data divided by the number of simulations.

For calculation of event-triggered average, 8 frames of the averaged neuronal signal prior to each astrocyte event was summed over all events and divided by the number of events. The timing of the astrocyte events was then shuffled 100 times and the same calculation was performed. The mean of the event-triggered average and the shuffled version was used for statistical comparison.

Simultaneous IC and auditory cortex (AC) imaging analysis: Ten minutes of calcium imaging were selected manually for less movement of the animal from 50-minute movies. Widefield raw images were imported into MATLAB (MATHWORKS) and corrected for photobleaching by subtracting a fitted exponent from the signal. The right IC was cropped and used for detection of movement using efficient subpixel image registration (Guizar-Sicairos et al., 2008). Image intensities were normalized as $\Delta F/F_o$ values as described above. An ellipse was manually drawn around the right IC and the average calcium trace within the ROI was calculated. The calcium trace was then smoothed and filtered by regressing the baseline over multiple shifted windows using a spline approximation (‘msbackadj’ function in MATLAB, window and step size – 20 frames). Movement related time-points were zeroed. A correlation was calculated between the IC signal and every pixel of the image to generate the map seen in Figure 2A. The correlation image was used to manually draw an ROI around auditory cortex and the resulting calcium signal was calculated, smoothed and filtered as described above. Pearson’s correlation coefficients were calculated between the IC and AC calcium signals. Cross correlations between the IC and AC mean-subtracted calcium signals were calculated and normalized so that the autocorrelations at zero lag equaled 1. Peaks in the calcium signals were detected in MATLAB using the built-in peak detection function (‘findpeaks’) using a fixed value threshold criterion (1% $\Delta F/F_o$).

For the images in Figure 2D, seed ROIs were placed across the future tonotopic axis of the IC manually and fluorescent signals normalized as described above and mean subtracted. For each IC ROI, a correlation was calculated between the calcium signal and all the pixels in a cropped movie which included the IC or the AC. The maps were then combined into RGB channels with the color-coding denoting different active areas.

AC imaging analysis: Widefield raw images were imported into MATLAB (MATHWORKS) and corrected for photobleaching by subtracting a fitted exponent from the signal. Images were cropped to include $1500–1900^2$ μm^2 of auditory cortex. Image intensities were normalized as $\Delta F/F_o$ values, where $\Delta F = F - F_o$ and F_o was defined as the median over all frames. Grid ROIs were defined as $30–50^2$ pixels over the cropped image, resulting in 25 ROIs for each movie. The calcium trace for each ROI was smoothed and filtered by regressing the baseline over multiple shifted windows using a spline approximation (‘msbackadj’ function in MATLAB, window and step size - 20 frames). Movement was detected using efficient subpixel image registration (Guizar-Sicairos et al., 2008) and the signal was zeroed during the detected movement events. Peaks in the calcium signals were detected in MATLAB using the built-in peak detection function (‘findpeaks’) using a threshold criterion for the minimum prominence of median + 3*MAD for each ROI. The minimum peak width was defined as 20 frames for P4 and P14–15 and 10 frames for P7

and P11 (this was because events at these latter ages were more focal and faster). Peaks that were detected within 20 frames of each other were defined as one event. The detected events were manually inspected against the ΔF movie and those that were clearly associated with movement (that were undetected by the algorithm), were manually removed.

Sound evoked imaging analysis: Widefield epifluorescence videos of evoked responses in IC or AC underwent bleach correction and normalization (10^{th} percentile) as $\Delta F/F_o$ values in MATLAB, as described above for widefield imaging of spontaneous neuronal and astrocyte activity. For dual-color imaging, videos of evoked neuronal and astrocyte activity were processed identically. Image segments were separated by stimulus frequency, aligned from 1 s prior to and 3 s following tone presentation, and averaged across the 4 presentations of each tone. For calculation of $\Delta F/F_o$ responses, a circular ROI (250 pixel diameter) was placed over auditory cortex after visualization of averaged neuronal pure tone responses to all stimuli (dual-color imaging) or local vasculature patterns (astrocyte imaging alone). Normalized and averaged responses from tone onset to 1 s following tone offset were used for display purposes.

Acute brain slice preparation: Mice were swiftly decapitated and their brains were dissected out and mounted on a vibratome (Leica VT100S) equipped with a sapphire blade. IC slices 250 μm thick were cut in ice-cold N-methyl-D-glucamine (NMDG) based cutting solution, containing (in mM): 135 NMDG, 1 KCl, 1.2 KH_2PO_4, 1.5 $MgCl_2$, 0.5 $CaCl_2$, 10 Dextrose, 20 Choline Bicarbonate, (pH 7.4). IC slices were then transferred to artificial cerebral spinal fluid (ACSF) containing (in mM): 119 NaCl, 2.5 KCl, 2.5 $CaCl_2$, 1.3 $MgCl_2$, 1 NaH_2PO_4, 26.2 $NaHCO_3$, and 11 Dextrose (292–298 mOsm/L) and were maintained at 37°C for 40 min, and at room temperature thereafter. Both NMDG solution and ACSF were bubbled continuously with 95% O_2/5% CO_2. All slice imaging experiments were carried out at room temperature.

Pharmacological manipulations: To minimize the influence of neuronal activity on astrocyte calcium signals in slices, all pharmacological manipulations were performed in Tetrodotoxin citrate (TTX; Na_v antagonist, Alomone labs, 1 μM), unless otherwise noted. In some cases, agonists were applied in the presence of (RS)-CPP (NMDA antagonist, Tocris, 10 μM), and NBQX disodium salt (AMPA antagonist, Tocris, 10 μM) in addition to TTX. In most cases, imaging began with 5 minutes of ACSF and then 5 minutes of TTX perfusion of the slice. Since the activity in these conditions were not significantly different, they were averaged and called ‘Baseline’ for presentation and statistical testing. To activate metabotropic receptors 5 and 3, (S)-3,5-Dihydroxyphenylglycine (DHPG; group I metabotropic glutamate receptor agonist, Tocris, 10 μM) or LY354740 (group II metabotropic receptor agonist, Tocris, 1 μM) were dissolved in ASCF and applied through the superfusing solution. To ensure their specificity, after a 15 min wash, the agonists were applied in the presence of their antagonists: MPEP hydrochloride (an mGluR5 specific antagonist, Tocris, 10 μM) and LY341495 (an mGluR2/3 antagonist, Tocris, 100 μM). In the case of the mGluR5-cKO mice, Norepinephrine (NE; Sigma, 10 μM) was puffed onto the slice at the end of the experiment to ensure that astrocytes were able to respond reliably with increases in calcium (see Figure 3C). In a subset of experiments, we distinguished between

the central nucleus of the IC and the external cortex of the IC using the developing mouse brain atlas and compared the response to the group II agonist LY354740.

Time-lapse fluorescence imaging in acute brain slices: GCaMP in IC astrocytes was imaged using a Zeiss LSM 710 confocal microscope with 20x (NA 1.0) water immersion objective (Zeiss), using the 488 nm laser line. Slices were continuously superfused with ACSF bubbled with 95% O_2/5% CO_2. Astrocytes were imaged at a low laser power of <1 mW, with no pixel averaging, high PMT gain (>750), and with a pinhole size of 1–2.5 airy units, corresponding to 1.6 – 3.6 μm of z-depth. Astrocytes were imaged at a pixel depth of 8 bit with a resolution of 512 × 512 pixels over 600 frames at a frame scan rate of 2 Hz.

Image processing for acute brain slice: Images were processed first with Fiji and then with MATLAB. The individual movies for each condition (baseline, agonist, agonist+antagonist, etc.) were loaded for one slice and concatenated. The resulting movie was visually inspected to make sure that no substantial drift occurred. If there was a drift in the Z-plane, the movie was discarded and not used for further analysis. For X-Y drift, the movie was registered in Fiji using the 'MultiStackReg' plugin (Thevenaz and Unser, 1998) with a Rigid body transformation, aligning it to the first image in the baseline condition. The concatenated movie was then opened in MATLAB and corrected for photobleaching by subtracting a fitted exponent from the signal. Grid ROIs were defined for each slice separately based on the magnification used so that each square was between $(15–25)^2$ μm. For each grid ROI, the $\Delta F/F_0$ was calculated, where F was the averaged signal over all pixels in the ROI and F_0 was defined as the median over all frames. The calcium trace was then smoothed and filtered by regressing the baseline over multiple shifted windows using a spline approximation ('msbackadj' function in MATLAB, window and step size - 45 frames). To define responsive grid ROIs, peaks in the signal were detected using the built-in 'findpeaks' function in MATLAB. The threshold was defined for each ROI as the median + 5xMAD of the signal. Area under the curve was calculated with a trapezoidal numerical integration algorithm ('trapz' in MATLAB) within a user-defined 'On time' when the response was visible in the agonist condition.

Immunohistochemistry: Mice were deeply anesthetized with isoflurane and perfused with freshly prepared 4% paraformaldehyde (PFA) in 0.1M phosphate buffered saline (PBS). Brains were isolated and post-fixed in 4% PFA at least 4 hours at 4°C and stored at 4°C in PBS or 30% Sucrose until processing. Brains were frozen in Tissue-Tek O.C.T. (Sakura) and cut on a cryostat microtom (Microm HM550; Thermo Fisher Scientific) into 35–50 μm sagittal or coronal sections. Before immunostaining, free-floating sections were rinsed 3x for 5 min each in PBS, then incubated for 1 hr at RT in a blocking buffer (0.3% Triton X-100 and 5% normal donkey serum in PBS). For immunolabeling, sections were incubated with primary antibodies diluted in blocking buffer overnight at 4°C on an orbital shaker. After rinsing at RT with PBS 3x for 10 min each, sections were incubated on an orbital shaker with fluorescent dye-conjugated secondary antibodies diluted in blocking buffer for 2–3 hr at RT. The sections were then rinsed 3x in PBS for 5 min each (during the second rinse, DAPI was added to the PBS at 1:2500 for nuclear staining) and then mounted on

charged glass-slides and cover-slipped in Aqua Ploy/Mount (Polysciences, Inc.). Primary antibodies used: chicken anti-GFP (1:4000, Aves Lab, Inc.), mouse anti-NeuN (1:500, Millipore), mouse anti-S100 (β-Subunit) (1:400, Sigma-Aldrich). Secondary antibodies (raised in donkey): Alexa Fluor 488-, Alexa Fluor 546-, conjugated secondary antibodies to chicken or mouse (1:1000, Thermo Fisher Scientific and Jackson ImmunoResearch). Images were acquired using a Zeiss LSM 800 confocal microscope with a 20x (Plan-Apochromat, Zeiss) or 63x (Plan-Apochromat, Zeiss) oil immersion objectives, and the pinhole set to 1 airy unit. Images were then opened with Fiji and brightness and contrast levels were adjusted. The images were pseudocolored when two or more channels were merged.

Quantification and statistical analyses

Statistics were performed in MATLAB (Mathworks) or in Excel (Microsoft). All statistical details, including the exact value of n, what n represents, and which statistical test was performed, can be found in the figure legends or in the results section. Unless otherwise noted, data are presented as mean ± standard error of the mean. All datasets were tested for Gaussian normality using the Lilliefors test (this test was chosen because it does not require specification of the null distribution). If datasets were normal, two-tailed paired or unpaired t-tests were used. Before unpaired t-tests, the data was tested for equality of variance using the F-test. If normality was rejected, the nonparametric Wilcoxon test was used. For single comparisons, significance was defined as $p < 0.05$. When multiple comparisons were made, the Bonferroni correction was used to adjust p-values accordingly to lower the probability of type I errors. For multiple condition datasets with repeated measures (such as in Fig S4C,E,G), a linear mixed effect model was used with fixed effects defined as the different conditions tested and a random noise effect defined as the different slices. The significance was tested using an F-test on the coefficients. Post-hoc comparisons were corrected using the Bonferroni method. For comparison of various independent time points, such as in Fig 2F a one-way ANOVA was used with Tukey-Kramer post-hoc comparisons.

Supplementary Material

Refer to Web version on PubMed Central for supplementary material.

Acknowledgments

We thank Dr. M. Pucak and N. Ye for technical assistance, T. Shelly for machining expertise, and members of the Bergles laboratory for discussions and comments on the manuscript. We thank Dr. A. Agarwal for providing expertise in slice imaging. V.K., T.A.B. and C.J.K. were supported by NRSA grants from the NIH (F32DC017364, F31DC016497 and F30DC018711, respectively). Funding was provided by grants from the NIH (DC008060, NS050274, DC000023, and EY017203), and a grant from the Rubenstein Fund for Hearing Research to D.B.

References

Ackman JB, Burbridge TJ, and Crair MC (2012). Retinal waves coordinate patterned activity throughout the developing visual system. Nature 490, 219–225. [PubMed: 23060192]

Agarwal A, Wu P-H, Hughes EG, Fukaya M, Tischfield MA, Langseth AJ, Wirtz D, and Bergles DE (2017). Transient Opening of the Mitochondrial Permeability Transition Pore Induces Microdomain Calcium Transients in Astrocyte Processes. Neuron 93, 587–605.e7. [PubMed: 28132831]

Allen NJ, Bennett ML, Foo LC, Wang GX, Chakraborty C, Smith SJ, and Barres BA (2012). Astrocyte glypicans 4 and 6 promote formation of excitatory synapses via GluA1 AMPA receptors. Nature 486, 410–414. [PubMed: 22722203]

Araque A, Li N, Doyle RT, and Haydon PG (2000). SNARE protein-dependent glutamate release from astrocytes. J. Neurosci. 20, 666–673. [PubMed: 10632596]

Araque A, Carmignoto G, Haydon PG, Oliet SHR, Robitaille R, and Volterra A. (2014). Gliotransmitters Travel in Time and Space. Neuron 81, 728–739. [PubMed: 24559669]

Babola TA, Li S, Gribizis A, Lee BJ, Issa JB, Wang HC, Crair MC, and Bergles DE (2018). Homeostatic Control of Spontaneous Activity in the Developing Auditory System. Neuron 99, 511–524.e5. [PubMed: 30077356]

Babola TA, Li S, Wang Z, Kersbergen CJ, Elgoyhen AB, Coate TM, and Bergles DE (2021). Purinergic Signaling Controls Spontaneous Activity in the Auditory System throughout Early Development. J. Neurosci. 41, 594–612. [PubMed: 33303678]

Barres BA, Koroshetz WJ, Chun LLYY, and Corey DR (1990). Ion channel expression by white matter glia: The type-1 astrocyte. Neuron 5, 527–544. [PubMed: 1698397]

Bayer SA, and Altman J. (1991). Neocortical Development (New York: Raven Press).

Bergles DE, and Jahr CE (1997). Synaptic activation of glutamate transporters in hippocampal astrocytes. Neuron 19, 1297–1308. [PubMed: 9427252]

Blanco-Suarez E, Liu T-FF, Kopelevich A, and Allen NJ (2018). Astrocyte-Secreted Chordin-like 1 Drives Synapse Maturation and Limits Plasticity by Increasing Synaptic GluA2 AMPA Receptors. Neuron 100, 1116–1132.e13. [PubMed: 30344043]

Blankenship AG, and Feller MB (2010). Mechanisms underlying spontaneous patterned activity in developing neural circuits. Nat. Rev. Neurosci. 11, 18–29. [PubMed: 19953103]

Bushong EA, Martone ME, and Ellisman MH (2004). Maturation of astrocyte morphology and the establishment of astrocyte domains during postnatal hippocampal development. Int. J. Dev. Neurosci. 22, 73–86. [PubMed: 15036382]

Cai Z, Schools GP, and Kimelberg HK (2000). Metabotropic glutamate receptors in acutely isolated hippocampal astrocytes: Developmental changes of mGluR5 mRNA and functional expression. 29, 70–80.

Christopherson KS, Ullian EM, Stokes CCA, Mullowney CE, Hell JW, Agah A, Lawler J, Mosher DF, Bornstein P, and Barres BA (2005). Thrombospondins are astrocyte-secreted proteins that promote CNS synaptogenesis. Cell 120, 421–433. [PubMed: 15707899]

Chung W-S, Clarke LE, Wang GX, Stafford BK, Sher A, Chakraborty C, Joung J, Foo LC, Thompson A, Chen C, et al. (2013). Astrocytes mediate synapse elimination through MEGF10 and MERTK pathways. Nature 504, 394–400. [PubMed: 24270812]

Clarke LE, and Barres BA (2013). Emerging roles of astrocytes in neural circuit development. Nat. Rev. Neurosci. 14, 311–321. [PubMed: 23595014]

Clause A, Kim G, Sonntag M, Weisz CJC, Vetter DE, Rűbsamen R, and Kandler K. (2014). The Precise Temporal Pattern of Prehearing Spontaneous Activity Is Necessary for Tonotopic Map Refinement. Neuron 82, 822–835. [PubMed: 24853941]

Cornell-bell AAH, Finkbeiner SM, Cooper MS, Stephen J, Finkbeiner SM, Cooper MS, Ephrussi A, Church GM, Tonegawa S, and Smith SJ (1990). Glutamate Induces Calcium Waves in Cultured Astrocytes : Long-Range. Science (80-.). 247, 470–473.

Cornell-Bell AH, Thomas PG, and Smith SJ (1990). The excitatory neurotransmitter glutamate causes filopodia formation in cultured hippocampal astrocytes. Glia 3, 322–334. [PubMed: 1699891]

Dana H, Mohar B, Sun Y, Narayan S, Gordus A, Hasseman JP, Tsegaye G, Holt GT, Hu A, Walpita D, et al. (2016). Sensitive red protein calcium indicators for imaging neural activity. Elife 5.

Ding F, O'Donnell J, Thrane AS, Zeppenfeld D, Kang H, Xie L, Wang F, and Nedergaard M. (2013). α1-Adrenergic receptors mediate coordinated Ca2+ signaling of cortical astrocytes in awake, behaving mice. Cell Calcium 54, 387–394. [PubMed: 24138901]

Durkee CA, Covelo A, Lines J, Kofuji P, Aguilar J, and Araque A. (2019). G i/o protein-coupled receptors inhibit neurons but activate astrocytes and stimulate gliotransmission. Glia 67, 1076–1093. [PubMed: 30801845]

Eroglu Ç, Allen NJ, Susman MW, O'Rourke NA, Park CY, Özkan E, Chakraborty C, Mulinyawe SB, Annis DS, Huberman AD, et al. (2009). Gabapentin Receptor α2δ−1 Is a Neuronal Thrombospondin Receptor Responsible for Excitatory CNS Synaptogenesis. Cell 139, 380–392. [PubMed: 19818485]

Freeman MR (2010). Specification and morphogenesis of astrocytes. Science (80-.). 330, 774–778.

Ghosh A, and Greenberg ME (1995). Calcium signaling in neurons: Molecular mechanisms and cellular consequences. Science (80-.). 268, 239–247.

Grosche J, Matyash V, Möller T, Verkhratsky A, Reichenbach A, and Kettenmann H. (1999). Microdomains for neuron-glia interaction: parallel fiber signaling to Bergmann glial cells. Nat. Neurosci. 2, 139–143. [PubMed: 10195197]

Guizar-Sicairos M, Thurman ST, and Fienup JR (2008). Efficient subpixel image registration algorithms. Opt. Lett. 33, 156. [PubMed: 18197224]

Haeffele BD, Young ED, and Vidal R. (2014). Structured Low-Rank Matrix Factorization: Optimality, Algorithm, and Applications to Image Processing. (PMLR), pp. 2007–2015.

Issa JB, Haeffele BD, Agarwal A, Bergles DE, Young ED, and Yue DT (2014). Multiscale Optical Ca2+ Imaging of Tonal Organization in Mouse Auditory Cortex. Neuron 83, 944–959. [PubMed: 25088366]

Katz B, and Miledi R. (1967). A study of synaptic transmission in the absence of nerve impulses. J. Physiol. 192, 407–436. [PubMed: 4383089]

Kim YS, Anderson M, Park K, Zheng Q, Agarwal A, Gong C, Saijilafu, Young LA, He S, LaVinka PC, et al. (2016). Coupled Activation of Primary Sensory Neurons Contributes to Chronic Pain. Neuron 91, 1085–1096. [PubMed: 27568517]

Kirkby LA, Sack GS, Firl A, and Feller MB (2013). A role for correlated spontaneous activity in the assembly of neural circuits. Neuron 80, 1129–1144. [PubMed: 24314725]

Lavialle M, Aumann G, Anlauf E, Pröls F, Arpin M, Derouiche A, Prols F, Arpin M, and Derouiche A. (2011). Structural plasticity of perisynaptic astrocyte processes involves ezrin and metabotropic glutamate receptors. Proc Natl Acad Sci U S A 108, 12915–12919.

Li X, Zima AV, Sheikh F, Blatter LA, and Chen J. (2005). Endothelin-1-induced arrhythmogenic Ca2+ signaling is abolished in atrial myocytes of inositol-1,4,5-trisphosphate(IP3)-receptor type 2-deficient mice. Circ. Res. 96, 1274–1281. [PubMed: 15933266]

Lippe WR (1994). Rhythmic spontaneous activity in the developing avian auditory system. J. Neurosci. 14, 1486–1495. [PubMed: 8126550]

Madisen L, Garner AR, Shimaoka D, Chuong AS, Klapoetke NC, Li L, van der Bourg A, Niino Y, Egolf L, Monetti C, et al. (2015). Transgenic mice for intersectional targeting of neural sensors and effectors with high specificity and performance. Neuron 85, 942–958. [PubMed: 25741722]

Mateo Z, and Porter JT (2007). Group II metabotropic glutamate receptors inhibit glutamate release at thalamocortical synapses in the developing somatosensory cortex. Neuroscience 146, 1062–1072. [PubMed: 17418955]

McLaughlin T, Torborg CL, Feller MB, and O'Leary DDM (2003). Retinotopic map refinement requires spontaneous retinal waves during a brief critical period of development. Neuron 40, 1147–1160. [PubMed: 14687549]

Di Menna L, Joffe ME, Iacovelli L, Orlando R, Lindsley CW, Mairesse J, Gressèns P, Cannella M, Caraci F, Copani A, et al. (2018). Functional partnership between mGlu3 and mGlu5 metabotropic glutamate receptors in the central nervous system. Neuropharmacology 128, 301–313. [PubMed: 29079293]

Moldrich RX, Apricó K, Diwakarla S, O'Shea RD, and Beart PM (2002). Astrocyte mGlu2/3-mediated cAMP potentiation is calcium sensitive: Studies in murine neuronal and astrocyte cultures. Neuropharmacology 43, 189–203. [PubMed: 12213273]

Morel L, Higashimori H, Tolman M, and Yang Y. (2014). VGluT1+ Neuronal Glutamatergic signaling regulates postnatal developmental maturation of cortical protoplasmic astroglia. J. Neurosci. 34, 10950–10962.

Nedergaard M. (1994). Direct signaling from astrocytes to neurons in cultures of mammalian brain cells. Science (80-.). 263, 1768–1771.

Paukert M, Agarwal A, Cha J, Doze VA, Kang JU, and Bergles DE (2014). Norepinephrine controls astroglial responsiveness to local circuit activity. Neuron 82, 1263–1270. [PubMed: 24945771]

Petralia RS, Wang YX, Niedzielski AS, and Wenthold RJ (1996). The metabotropic glutamate receptors, MGLUR2 and MGLUR3, show unique postsynaptic, presynaptic and glial localizations. Neuroscience 71, 949–976. [PubMed: 8684625]

Petravicz J, Fiacco TA, and McCarthy KD (2008). Loss of IP3 receptor-dependent Ca2+ increases in hippocampal astrocytes does not affect baseline CA1 pyramidal neuron synaptic activity. J. Neurosci. 28, 4967–4973. [PubMed: 18463250]

Porter JT, and McCarthy KD (1995). GFAP-positive hippocampal astrocytes in situ respond to glutamatergic neuroligands with increases in [Ca2+]i. Glia 13, 101–112. [PubMed: 7544323]

Scanziani M, Salin PA, Vogt KE, Malenka RC, and Nicoll RA (1997). Use-dependent increases in glutamate concentration activate presynaptic metabotropic glutamate receptors. Nature 385, 630–634. [PubMed: 9024660]

Schindelin J, Arganda-Carreras I, Frise E, Kaynig V, Longair M, Pietzsch T, Preibisch S, Rueden C, Saalfeld S, Schmid B, et al. (2012). Fiji: An open-source platform for biological-image analysis. Nat. Methods 9, 676–682. [PubMed: 22743772]

Slezak M, Kandler S, Van Veldhoven PP, Van den Haute C, Bonin V, and Holt MG (2019). Distinct Mechanisms for Visual and Motor-Related Astrocyte Responses in Mouse Visual Cortex. Curr. Biol. 29, 3120–3127.e5. [PubMed: 31495587]

Srinivasan R, Huang BS, Venugopal S, Johnston AD, Chai H, Zeng H, Golshani P, and Khakh BS (2015). Ca(2+) signaling in astrocytes from Ip3r2(−/−) mice in brain slices and during startle responses in vivo. Nat. Neurosci. 18, 708–717. [PubMed: 25894291]

Stogsdill JA, Ramirez J, Liu D, Kim YH, Baldwin KT, Enustun E, Ejikeme T, Ji RR, and Eroglu C. (2017). Astrocytic neuroligins control astrocyte morphogenesis and synaptogenesis. Nature 551, 192–197. [PubMed: 29120426]

Sun W, McConnell E, Pare J-F, Xu Q, Chen M, Peng W, Lovatt D, Han X, Smith Y, and Nedergaard M. (2013). Glutamate -Dependent Neuroglial Calcium Signaling Differs Between Young and Adult Brain. Science (80-.). 339, 197–200.

Sutherland ML, Delaney TA, and Noebels JL (1996). Glutamate transporter mRNA expression in proliferative zones of the developing and adult murine CNS. J. Neurosci. 16, 2191–2207. [PubMed: 8601800]

Swanson RA, Liu J, Miller JW, Rothstein JD, Farrell KA, Stein B, and Longuemare MC (1997). Neuronal Regulation of Glutamate Transporter Subtype Expression in Astrocytes. J. Neurosci. 17.

Tanabe Y, Nomura A, Masu M, Shigemoto R, Mizuno N, and Nakanishi S. (1993). Signal transduction, pharmacological properties, and expression patterns of two rat metabotropic glutamate receptors, mGluR3 and mGluR4. J. Neurosci. 13, 1372–1378. [PubMed: 8463825]

Thevenaz P, and Unser M. (1998). Efficient mutual information optimizer for multiresolution image registration. In IEEE International Conference on Image Processing, pp. 833–837.

Tritsch NX, Yi E, Gale JE, Glowatzki E, and Bergles DE (2007). The origin of spontaneous activity in the developing auditory system. Nature 450, 50–55. [PubMed: 17972875]

Tritsch NX, Rodríguez-Contreras A, Crins TTH, Wang HC, Borst JGG, and Bergles DE (2010). Calcium action potentials in hair cells pattern auditory neuron activity before hearing onset. Nat. Neurosci. 13, 1050–1052. [PubMed: 20676105]

Ullian EM (2001). Control of Synapse Number by Glia. Science (80-.). 291, 657–661.

Wang T, Pentyala S, Rebecchi MJ, and Scarlata S. (1999). Differential association of the pleckstrin homology domains of phospholipases C-β1, C-β2, and C-δ1 with Lipid bilayers and the βγ Subunits of heterotrimeric G proteins. Biochemistry 38, 1517–1524. [PubMed: 9931017]

Wang X, Lou N, Xu Q, Tian G-F, Peng WG, Han X, Kang J, Takano T, and Nedergaard M. (2006). Astrocytic Ca2+ signaling evoked by sensory stimulation in vivo. Nat. Neurosci. 9, 816–823. [PubMed: 16699507]

Wang Y, Rattner A, Zhou Y, Williams J, Smallwood PM, and Nathans J. (2012). Norrin/Frizzled4 signaling in retinal vascular development and blood brain barrier plasticity. Cell 151, 1332–1344. [PubMed: 23217714]

Winchenbach J, Düking T, Berghoff SA, Stumpf SK, Hülsmann S, Nave KA, and Saher G. (2016). Inducible targeting of CNS astrocytes in Aldh1l1-CreERT2 BAC transgenic mice. F1000Research 5.

Winder D, and Conn P. (1993). Activation of metabotropic glutamate receptors increases cAMP accumulation in hippocampus by potentiating responses to endogenous adenosine. J. Neurosci. 13, 38–44. [PubMed: 8380851]

Xi ZX, Baker DA, Shen H, Carson DS, and Kalivas PW (2002). Group II metabotropic glutamate receptors modulate extracellular glutamate in the nucleus accumbens. J. Pharmacol. Exp. Ther. 300, 162–171. [PubMed: 11752112]

Xu H, Furman M, Mineur YS, Chen H, King SL, Zenisek D, Zhou ZJ, Butts DA, Tian N, Picciotto MR, et al. (2011). An Instructive Role for Patterned Spontaneous Retinal Activity in Mouse Visual Map Development. Neuron 70, 1115–1127. [PubMed: 21689598]

Xu J, Zhu Y, Contractor A, and Heinemann SF (2009). mGluR5 Has a Critical Role in Inhibitory Learning. J. Neurosci. 29.

Yang Y, Gozen O, Watkins A, Lorenzini I, Lepore A, Gao Y, Vidensky S, Brennan J, Poulsen D, Won Park J, et al. (2009). Presynaptic Regulation of Astroglial Excitatory Neurotransmitter Transporter GLT1. Neuron 61, 880–894. [PubMed: 19323997]

Yu X, Taylor AMW, Nagai J, Golshani P, Evans CJ, Coppola G, and Khakh BS (2018). Reducing Astrocyte Calcium Signaling In Vivo Alters Striatal Microcircuits and Causes Repetitive Behavior. Neuron 99, 1170–1187.e9. [PubMed: 30174118]

Zhang Y, Chen K, Sloan SA, Bennett ML, Scholze AR, O'Keeffe S, Phatnani HP, Guarnieri P, Caneda C, Ruderisch N, et al. (2014). An RNA-sequencing transcriptome and splicing database of glia, neurons, and vascular cells of the cerebral cortex. J. Neurosci. 34, 11929–11947.

Zheng JQ, and Poo MM (2007). Calcium signaling in neuronal motility. Annu. Rev. Cell Dev. Biol. 23, 375–404. [PubMed: 17944572]

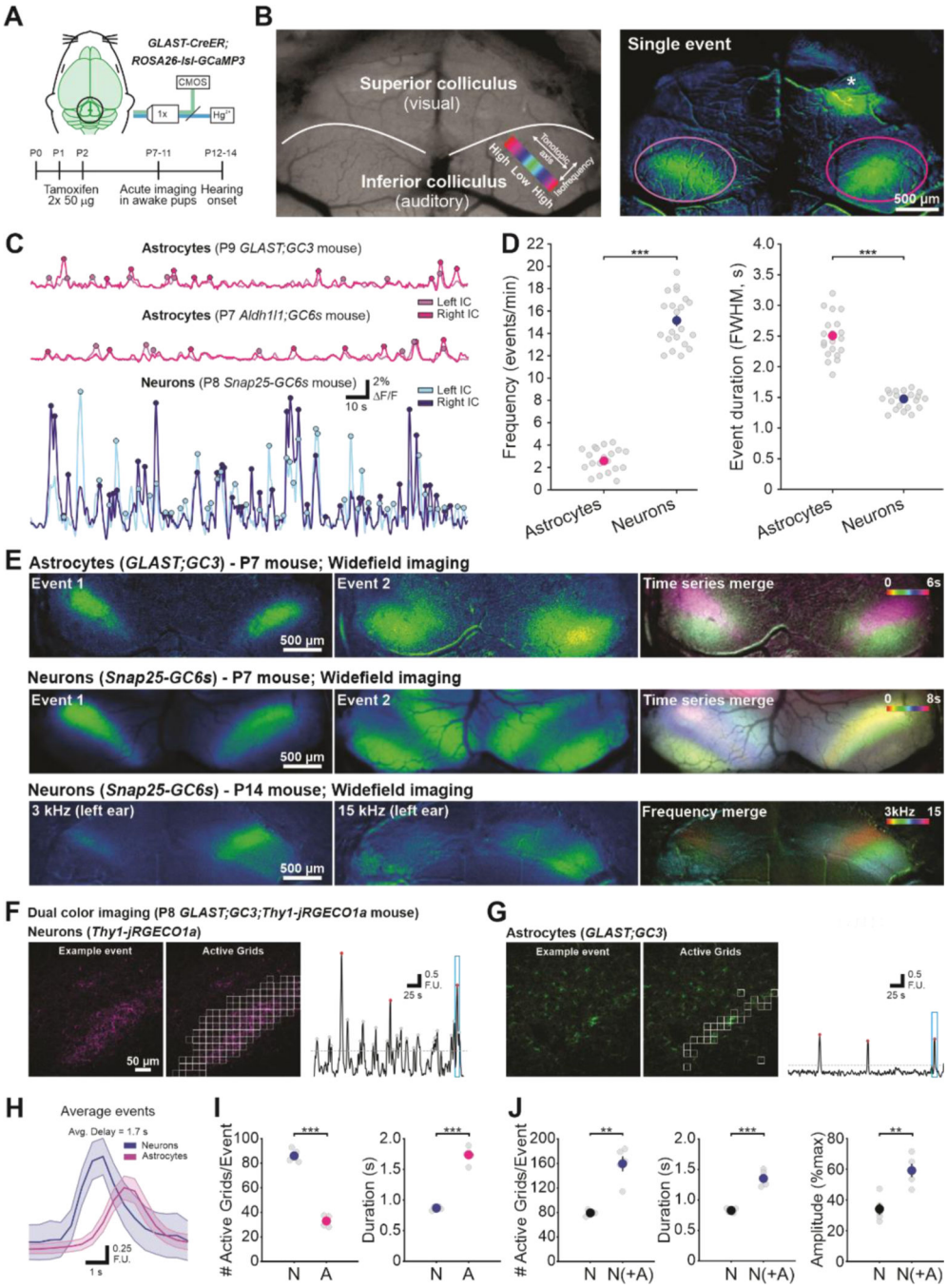

Figure 1. Coincident astrocyte-neuron calcium signaling in the inferior colliculus prior to hearing onset.

A. Configuration and timeline for widefield imaging of the midbrain of neonatal mice. **B**. Imaging field of view with superior (SC) and inferior (IC) colliculus denoted (*Left*). Tonotopic and isofrequency axes overlayed. *Right*, single astrocyte calcium event in left and right IC (ROI circles) and calcium wave in SC (asterisk) in a P9 *GLAST-CreER;ROSA26-lsl-GCaMP3* (*GLAST;GC3*) mouse. **C**. *Top*, astrocyte calcium transients (filled circles) from ROIs in B (ΔF/F). *Middle*, astrocyte calcium transients from a P7 *Aldh1l1-CreER;ROSA26-*

lsl-GCaMP6s (*Aldh1l1;GC6s*) mouse. *Bottom*, neuronal calcium transients in a P8 *Snap25-T2A-GCaMP6s* mouse **D**. Average frequency (*Left*) and duration of events (*Right;* Full width at half-maximum) for each mouse (gray circles). Colored circles denote the mean, error bars are SEMs (contained within the mean when not visible). Student's t-test (***p<0.001; n = 20 P7–9 and 21 P6–11 mice for astrocytes and neurons, respectively). **E**. Spatial localization of spontaneous astrocyte (*Top*) and neuronal (*Middle*) calcium events in the IC of P7 mice. *Bottom*, Sound-evoked neuronal calcium responses to 3 and 15kHz 100dB SPL tones presented to the left ear in a P13 mouse after hearing onset. *Right*, Color-coded representation of events over time (*Top* and *Middle*) and frequencies (*Bottom*; 3, 9.5, 15 and 20 kHz shown). Scale bar applies to all images. **F**–**I**. Simultaneous 2-photon imaging of astrocyte and neuron activity in a P8 *GLAST;GC3;Thy1-jRGECO1a* mouse. **F-G**. One calcium event (*Left*) and active ROIs (*Middle*, see Methods). *Right*, fluorescence changes for one ROI in the field (red circles - astrocyte associated events; gray circles - non-astrocyte associated events; dashed line - threshold) for neurons (**F**) and astrocytes (**G**). Cyan box marks event shown in left image. (F.U. = Fluorescence Units) **H**. Average calcium transients (mean ± SEMs (shaded)) of astrocyte and preceding neuronal events (n = 80 events from 5 P8 mice). **I**. Average number of active grids (*Left*) and duration of events (*Right*; measured as half prominence of the peak) between all neuronal events (N) and astrocyte events (A). **J**. Average number of active grids (*Left*), duration of events (*Middle)* and amplitude of events (*Right*; normalized to maximal values for each animal), between neuronal events not associated with astrocyte activation (N, black) and neuronal events associated with astrocyte activation (N(+A), blue). Student's t-test (**p<0.01, ***p<0.001; n = 5 P8 mice).

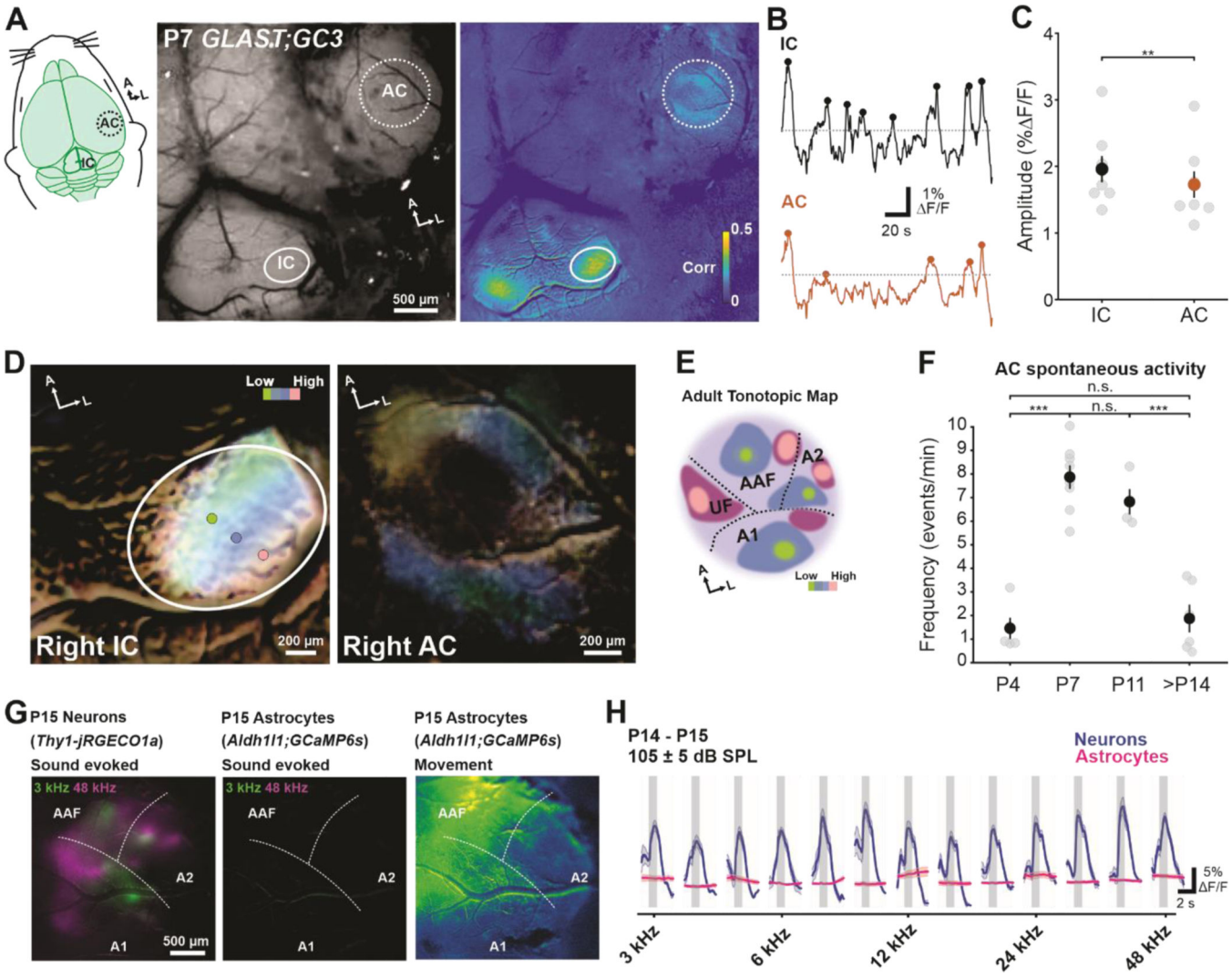

Figure 2. Coordinated astrocyte calcium activity occurs in the auditory cortex and is developmentally restricted.

A. Widefield imaging of IC and auditory cortex (AC) simultaneously in a P7 *GLAST;GC3* mouse (illustration in *Left,* imaging field of view in *Middle*). A=anterior; L=lateral. *Right*, correlation map generated by performing a pixel-by-pixel correlation with activity in IC (see Methods). **B**. Astrocyte calcium transients (filled circles) from ROIs in A. Dashed line denotes threshold. **C**. Average event amplitudes between IC and AC. Paired Student's t-test (**p<0.01; n = 8 P7–8 mice). **D**. Correlation activity maps between right IC and AC, from mouse shown in A. Calcium signals from seed ROIs on the IC movie (colored circles) were correlated to each pixel in AC and IC movies. Colors indicate pixels with high correlations with the seed ROIs, which resulted in segregated frequencies in IC (*Left*) and AC (*Right*). **E**. Tonotopic organization of the adult auditory cortex, adapted from Issa *et al.*, 2014. **F**. Average spontaneous astrocyte calcium event frequency in auditory cortex over different postnatal ages. One-way ANOVA, Post-hoc Tukey-Kramer (***p<0.001, n.s. = not significant; n = 5, 8, 4, 6 for P4, P7, P11, P14–15 mice, respectively). **G**. Sound-evoked widefield imaging in a P15 *Aldh1l1;GC6s;Thy1-jRGECO1a* mouse (105 ± 5dB SPL)

imaged separately for red and green channels. *Left*, color-coded map of neuronal responses to low (3kHz) and high (48kHz) frequency tones. *Middle*, no astrocyte responses to tone stimuli from the same animal. *Right*, astrocytes increased calcium during movement. Scale bar applies to all images. **H**. Mean ± SEM (shaded) of AC neurons (blue) and astrocytes (magenta) calcium responses to sound stimuli (gray bar) of different frequencies (105 ± 5 dB SPL) applied to the left ear in P14–15 *Aldh1l1;GC6s;Thy1-jRGECO1a* mice (n = 3 mice).

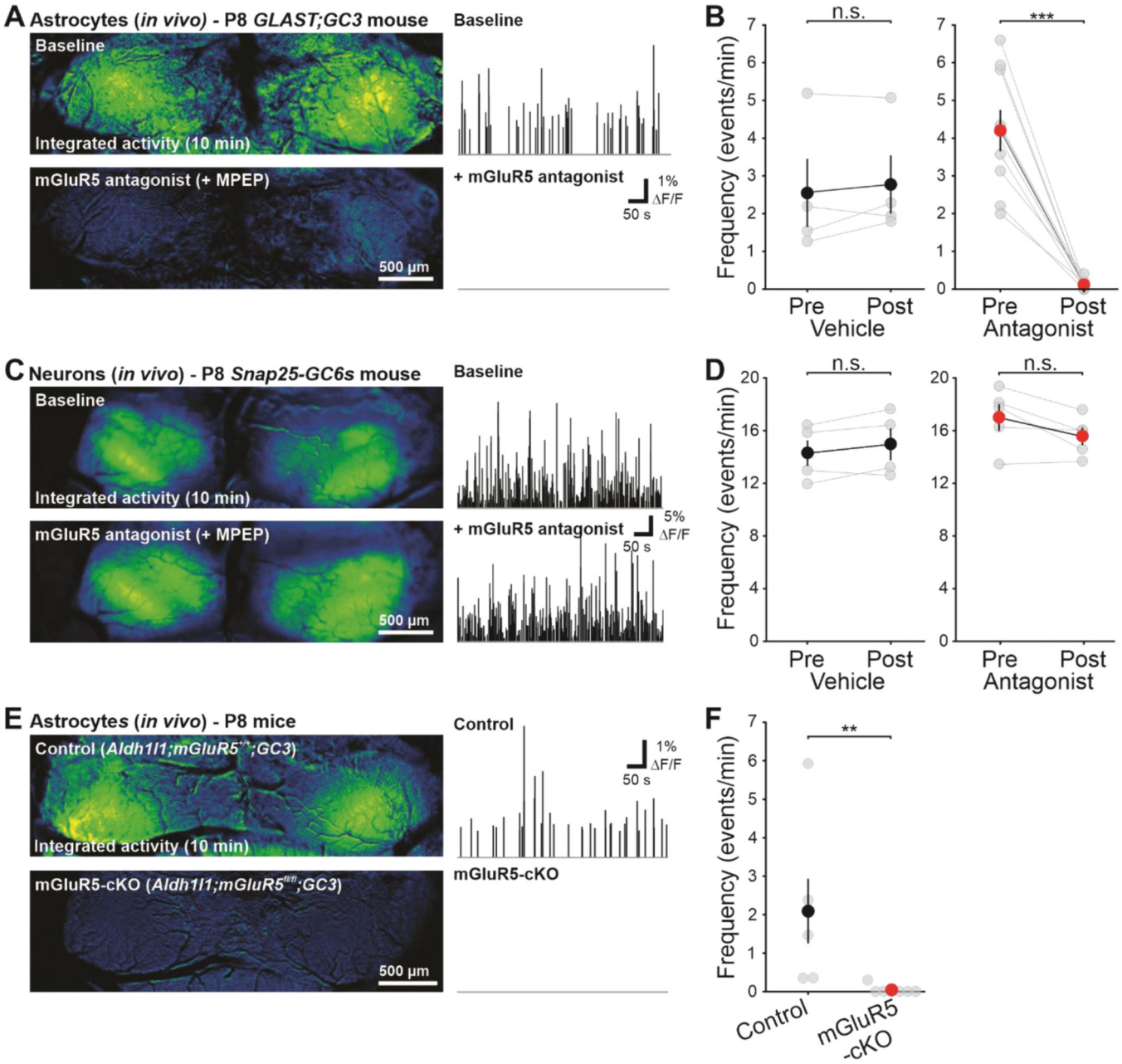

Figure 3. Astrocyte calcium events require mGluR5 receptors.

A. *Left*, maximum intensity image of all frames before (Baseline; *Top*) and 1 hour after (*Bottom*) systemic administration of MPEP (an mGluR5 antagonist) in a P8 *GLAST;GC3* mouse. *Right*, raster plot denoting detected peaks. **B**. Average frequency of events before and after administration of either vehicle (ddH_2O; *Left*) or MPEP (*Right*). Colored circles are mean ± SEM, gray circles are averages for each mouse. Paired t-test (n.s. = not significant, ***p<0.001; n = 4 and 9 P7–9 mice for vehicle and MPEP, respectively). **C**. *Left*, sum of all frames before (Baseline; *Top*) and 1 hour after (*Bottom*) systemic administration of MPEP in a P8 *Snap25-GC6s* mouse. *Right*, raster plot denoting detected peaks. **D**. Average frequency of events before and after administration of either vehicle

(*Left*) or MPEP (*Right*). Paired t-test (n.s. = not significant; n = 4 P6–8 mice and n = 5 P7–11 mice for vehicle and MPEP, respectively). **E**. *Left*, maximum intensity image of all frames from P8 control (*Top*; *Aldh1l1-creER;mGluR5*$^{+/+}$*;GC3*) and mGluR5-cKO (*Bottom*; *Aldh1l1-creER;mGluR5*$^{fl/fl}$*;GC3*) mice. *Right*, raster plot denoting detected peaks. **F**. Average frequency of events in control (*Aldh1l1;GC3*) and mGluR5-cKO mice. Wilcoxon rank sum test (**p<0.01; n = 6 P7–8 and 7 P8–9 mice for control and mGluR5-cKO, respectively). Note that two control animals had very low calcium activity and were extremely lethargic during imaging, suggesting slow recovery from anesthesia.

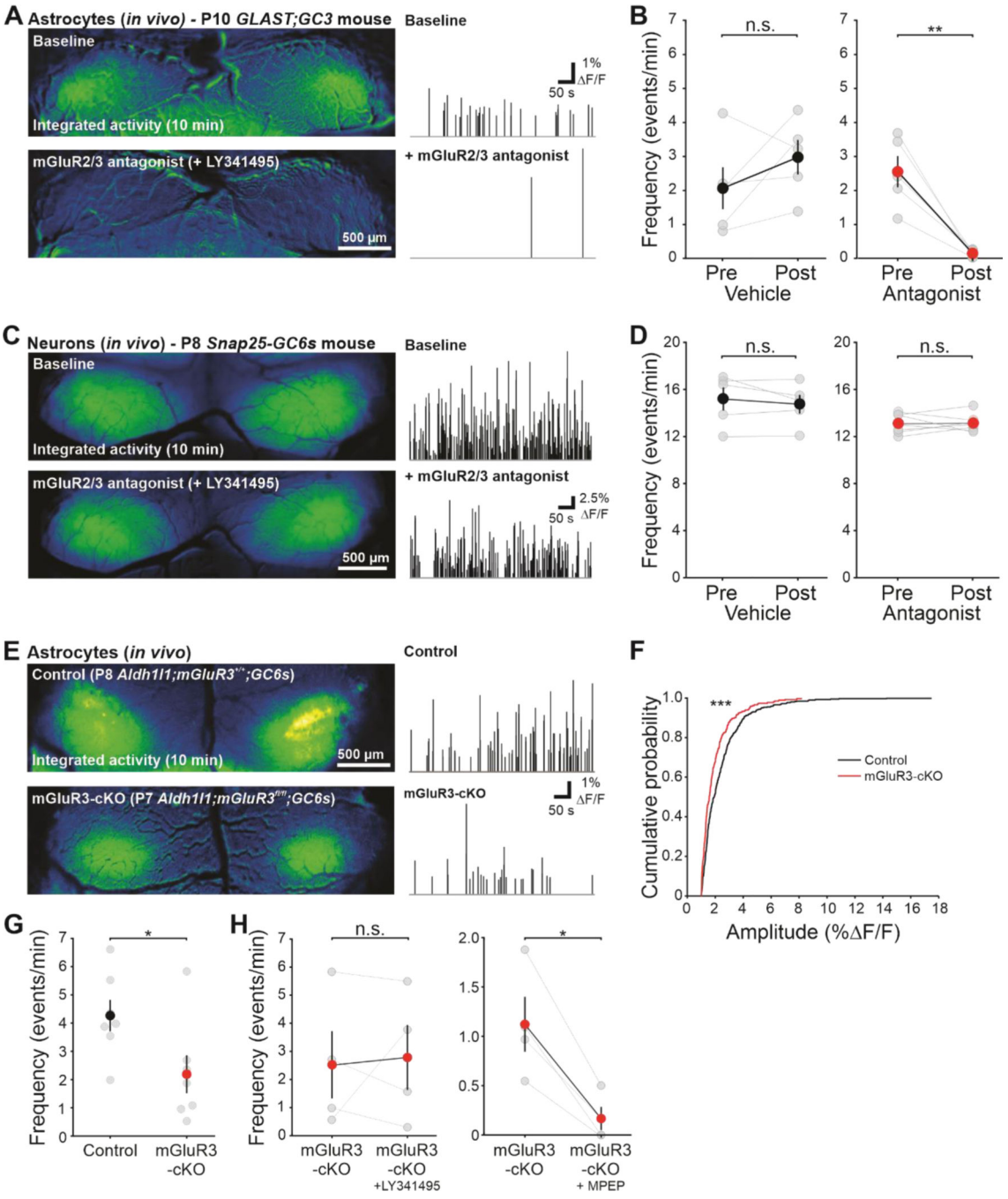

Figure 4. mGluR3 receptors contribute to *in vivo* astrocyte calcium events.

A. *Left*, maximum intensity image of all frames before (Baseline; *Top*) and 1 hour after (*Bottom*) systemic administration of LY341495 (an mGluR2/3 antagonist) in a P10 *GLAST;GC3* mouse. *Right*, raster plot denoting detected peaks. **B**. Average frequency of events in astrocytes before and after either vehicle (Saline; *Left*) or LY341495 injection (Antagonist; *Right*). Colored circles are mean ± SEM, gray circles are for each mouse. Paired t-test (n.s. = not significant, **p<0.01; n = 5 P7–9 mice and n = 5 P7–10 mice for vehicle and LY, respectively). **C**. *Left*, sum of all frames before (Baseline;

Top) and 1 hour after (*Bottom*) systemic administration of LY341495 in a P8 *Snap25-GC6s* mouse. *Right*, raster plot denoting detected peaks. **D**. Average frequency of events in neurons before and after either vehicle (*Left*) or LY341495 injection (Antagonist; *Right*). Paired t-test (n.s. = not significant; n = 5 P6–8 mice and n = 7 P7–8 mice for vehicle and LY, respectively). **E.** *Left*, maximum intensity image of all frames from P8 control (*Top*; *Aldh1l1-creER;mGluR3*$^{+/+}$*;GC6s*) and P7 mGluR3-cKO (*Bottom*; *Aldh1l1-creER;mGluR3*$^{fl/fl}$*;GC6s*) mice. *Right*, raster plot denoting detected peaks. **F**. Cumulative distribution of amplitudes over all events in control and mGluR3-cKO mice. Kolmogorov-Smirnov test (***p<0.001; n = 7 P7–8 and 6 P7–9 mice for control and mGluR3-cKO, respectively). **G**. Graph showing average frequency of events in control and mGluR3-cKO mice. Student's t-test, (*p < 0.05, n=7 and 6 mice for control and mGluR3-cKO, respectively). **H**. Graph showing lack of effect of systemic administration of LY341495 in mGluR3-cKO mice (*Left*; Paired t-test; n.s. = not significant, n = 4), and decrease in frequency of events following administration of an mGluR5 antagonist (MPEP; *Right*; Paired t-test; *p < 0.05, n = 4 mice).

KEY RESOURCES TABLE

REAGENT or RESOURCE	SOURCE	IDENTIFIER
Antibodies		
Normal Donkey Serum	Jackson ImmunoResearch Laboratories	Cat# 017-000-121 RRID: AB_2337258
Mouse polyclonal anti-NeuN	Millipore	Cat# MAB377; RRID: AB_2298772
Chicken polyclonal anti-GFP	Aves Labs	Cat# GFP-1020; RRID: AB_10000240
Mouse Monoclonal Anti-S-100 (β-Subunit) antibody	Sigma-Aldrich	Cat# S2532; RRID: AB_477499
Alexa Fluor 488-conjugated AffiniPure F(ab')$_2$ Fragment Donkey anti-chicken IgY (IgG)(H+L)	Jackson ImmunoResearch Laboratories	Cat# 703-546-155 RRID: AB_2340376
Donkey anti-mouse IgG (H+L), Alexa Fluor 546	ThermoFisher Scientific	Cat# A10036 RRID: AB_2534012
Chemicals, Peptides, and Recombinant Proteins		
(S)-3,5-Dihydroxyphenylglycine; DHPG	Tocris	Cat# 0805; CAS:162870-29-3
NBQX disodium salt	Tocris	Cat# 1044; CAS: 479347-86-9
Tetrodotoxin citrate	Alomone labs	Cat# T-550; CAS: 18660-81-6
(*RS*)-3-(2-Carboxypiperazin-4-yl)-propyl-1-phosphonic acid; (RS)-CPP	Tocris	Cat# 0173; CAS: 100828-16-8
2-Methyl-6-(phenylethynyl)pyridine hydrochloride; MPEP hydrochloride	Tocris	Cat# 1212; CAS: 219911-35-0
LY-354740	Tocris	Cat# 3246; CAS: 176199-48-7
LY-341495	Tocris	Cat# 1209; CAS: 201943-63-7
L-(-)-Norepinephrine (+)-bitartrate salt monohydrate	Sigma-Aldrich	Cat# A9512; CAS: 108341-18-0
Tamoxifen	Sigma-Aldrich	Cat# T5648; CAS:10540-29-1
(Z)-4-Hydroxytamoxifen	Sigma-Aldrich	Cat# H7904; CAS: 68047-06-3
Experimental Models: Organisms/Strains		
B6.Cg-*Snap25*$^{tm3.1Hze}$/J; *Snap25-T2A-GCaMP6s*	Jackson Laboratory	Stock# 025111
Tg(Slc1a3-cre/ERT)1Nat/J	Dr. Jeremy Nathans; Wang et al., 2012	IMSR_JAX:012586
B6;129-Gt(ROSA)26Sor(CAG-cGCaMP3)	Bergles lab; Paukert et al., 2014	N/A
Aldh1l1-CreERT2	Dr. Gesine Saher; Winchenbach et al., 2016	N/A
B6;129-Gt(ROSA)26Sor(CAG-cGCaMP6s)	Bergles lab; Kim et al., 2016	N/A
B6.129-*Grm5*$^{tm1.1Jixu}$/J	Dr. Paul Worley; Xu et al., 2009	IMSR Cat# JAX:028626
Grm3$^{tm1a(KOMP)Wtsi}$	KOMP; UC Davis	IMSR Cat# KOMP: CSD66285-1a-Wtsi
Itpr2^{tm1Chen}/Itpr2+	Dr. Ju Chen; Li et al., 2005	MGI Cat# 3713675
B6.129S4-*Gt(ROSA)26Sor*$^{tm1(FLP1)Dym}$/RainJ	Jackson Laboratory	Stock# 009086
Tg(Thy1-jRGECO1a)GP8.62Dkim/J	Jackson Laboratory	Stock# 030528
Oligonucleotides		
Primer: cccagttgagattggaaagtg (Snap25GC6s-com-s)	Jackson Laboratory	N/A
Primer: acttcgcacaggatccaaga (Snap25GC6s-mut-as)	Jackson Laboratory	N/A

REAGENT or RESOURCE	SOURCE	IDENTIFIER
Antibodies		
Primer: ctggttttgttggaatcagc (Snap25GC6s-wt-as)	Jackson Laboratory	N/A
Primer: tcaatgggcgggggtcgtt (CMV-E-as)	Paukert et al., 2014	N/A
Primer: ctctgctgcctcctggcttct (ROSA26 s)	Paukert et al., 2014	N/A
Primer: cgaggcggatcacaagcaata (ROSA26-as)	Paukert et al., 2014	N/A
Primer: gatgtcccacttacctgatgt (Grm5-1F1)	Xu et al., 2009	N/A
Primer: agttccgtgtctttattcttagc (Grm5-1R1)	Xu et al., 2009	N/A
Software and Algorithms		
ZEN Blue/Black	Zeiss	RRID:SCR_013672 https://www.zeiss.com/microscopy/us/products/microscope-software/zen.html#downloads
Fiji	Schindelin et al., 2012	RRID:SCR_003070 http://fiji.sc
MATLAB 2016b and 2019b	Mathworks	RRID: SCR_016098 https://www.mathworks.com/products/matlab.html
CorelDRAW Graphics Suite	Corel	RRID:SCR_001622 https://www.coreldraw.com/en/
MultiStackReg	Brad Busse	RRID:SCR_002285 http://bradbusse.net/sciencedownloads.html
Dftregistration code	Guizar-Sicairos et al., 2008	https://www.mathworks.com/matlabcentral/fileexchange/18401-efficient-subpixel-image-registration-by-cross-correlation?focused=6461818&tab=example
plot spread points (beeswarm plot)	Jonas (2020)	https://www.mathworks.com/matlabcentral/fileexchange/37105-plot-spread-points-beeswarm-plot
RANDBLOCK	Jos (10584) (2020)	https://www.mathworks.com/matlabcentral/fileexchange/17981-randblock
Custom codes used in this paper	Bergles lab	https://github.com/Bergles-lab/Kellner-et-al.−−2021-source-code